

Determination of the beam asymmetry Σ in η - and η' -photoproduction using Bayesian statistics

JAKOB MICHAEL KRAUSE

Masterarbeit in Physik

angefertigt im Helmholtz-Institut für Strahlen- und
Kernphysik

vorgelegt der

Mathematisch-Naturwissenschaftlichen Fakultät
der
Rheinischen Friedrich-Wilhelms-Universität
Bonn

Sep 2022

DRAFT

I hereby declare that this thesis was formulated by myself and that no sources or tools other than those cited were used.

Bonn,
Date
Signature

1. Gutachterin: JUN. PROF. DR. ANNIKA THIEL
2. Gutachter: PROF. DR. JOCHEN DINGFELDER

DRAFT

Contents

1	Introduction	1
1.1	Photoproduction of Pseudoscalar Mesons	4
1.2	Measurement of Polarization Observables	5
1.3	Introduction to BAYESIAN statistics	5
1.3.1	Frequentist Approach	5
1.3.2	Bayesian approach	5
1.4	Motivation and Structure of this Thesis	5
2	Experimental Setup	7
2.1	Production of (polarized) high energy photon beam	7
2.1.1	Tagger	8
2.2	Beam Target	8
2.3	Calorimeters	8
2.4	Trigger	8
3	Event selection	11
3.1	Preselection and charge cut	11
3.2	Time of particles	12
3.3	Kinematic constraints	14
3.3.1	Derivation of cut conditions	14
3.3.2	Determination of cut ranges	15
3.3.3	Quality of event selection	21
3.4	Investigation of background and additional cuts	22
3.4.1	Inspecting plausibility of background reactions	22
3.4.2	Misidentification of background reactions	25
3.4.3	Examination of additional cuts	28
3.5	Summary of event selection	31
4	Extraction of the beam asymmetries Σ_η and $\Sigma_{\eta'}$	33
4.1	Methods	34
4.1.1	Event yield asymmetries	34
4.1.2	Event based fit	37
4.2	Determination of Σ_η using Bayesian statistics	39
4.2.1	Application of methods to toy Monte Carlo data	40
4.2.2	Application of methods to data	48
4.2.3	Discussion	51

4.3	Determination of $\Sigma_{\eta'}$	55
4.3.1	Application of event based fit to toy Monte Carlo data	55
4.3.2	Application of event based fit to data	55
4.3.3	Systematic Error	55
5	Summary and outlook	45
A	Additional calculations	47
A.1	Statistical error for the asymmetry $A(\phi)$	47
B	Discussion of binned fits	49
	Bibliography	51
	List of Figures	55
	List of Tables	59

DRAFT

CHAPTER 4

Extraction of the beam asymmetries Σ_η and $\Sigma_{\eta'}$

The beam asymmetry Σ is observable when a linearly polarized photon beam and unpolarized liquid hydrogen target are employed. The polarized cross section $\frac{d\sigma}{d\Omega_{\text{pol}}}$ is not symmetric in the azimuthal angle ϕ anymore as opposed to the unpolarized cross section $\frac{d\sigma}{d\Omega_0}$. It is rather modulated by a cosine dependence which scales with the polarization observable Σ and the (linear) beam polarization p_γ , see equation (4.1) [San+11].

$$\frac{d\sigma}{d\Omega_{\text{pol}}} (E_\gamma, \cos \theta, \phi) = \frac{d\sigma}{d\Omega_0} (E_\gamma, \cos \theta) \cdot \left[1 - p_\gamma \Sigma (E_\gamma, \cos \theta) \cos (2\varphi) \right] \quad (4.1)$$

Since the incident photon beam is polarized, photon momentum \vec{k} and polarization $\vec{\epsilon}$ span a plane which is referred to as the beam polarization plane. This plane is tilted by the angle φ with respect to the reaction plane which is defined by the final state momenta. Naturally, this plane builds the angle ϕ in the laboratory system. At the same time the angle of the beam polarization plane in the same reference frame is defined as α . It holds

$$\varphi = \alpha - \phi. \quad (4.2)$$

Figure 4.1 illustrates definitions of all angles and planes. Theoretically the beam asymmetry can be

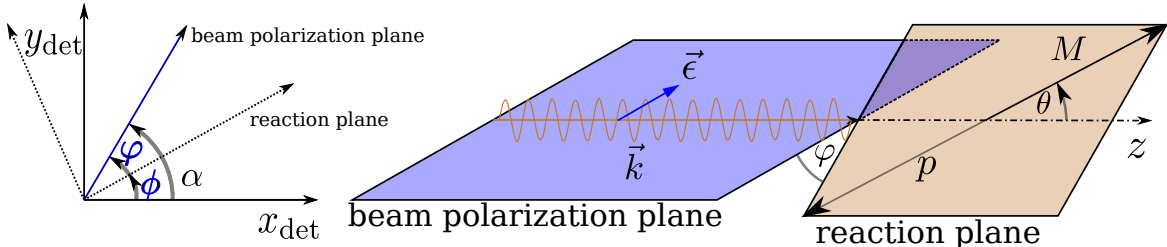


Figure 4.1: Left: Definition of angles α, ϕ, φ . Right: Photon momentum \vec{k} and polarization $\vec{\epsilon}$ define the beam polarization plane while the reaction plane is defined by the recoil proton p and produced meson M .

determined by a measurement of the cross section and a fit using equation (4.1). However, when calculating polarized cross sections, it is important to have good control over flux normalization and detector acceptance in three dimensions ($E_\gamma, \cos \theta, \phi$). To avoid this, the measurement of asymmetries

can be used to access the polarization observable Σ instead. Particularly, data is taken for two distinct orthogonal polarization settings corresponding to $\alpha = \pm 45^\circ$.

This chapter will illustrate the process of determining the beam asymmetry for η and η' photoproduction. The published results of Σ_η [Afz19; Afz+20] are used to check the accuracy and functionality of employed bayesian methods. Bayesian methods, as well as traditional frequentist approaches are used afterwards to extract new results for $\Sigma_{\eta'}$. First, the used methods will be presented and subsequently their application for each final state, respectively.

4.1 Methods

The beam asymmetry has to be determined via fits to ϕ distributions obtained from data. These are performed as either binned or unbinned fits. Both methods allow the application of Bayesian methods as will be discussed in the following. Additionally the advantages and disadvantages off all methods are compared.

4.1.1 Event yield asymmetries

Measurements were made in two distinct polarization settings $\alpha = \pm 45^\circ = \alpha^{\perp/\parallel}$. Thus, the polarized cross sections for both settings are given by¹

$$\frac{d\sigma^{\parallel}}{d\Omega_{\text{pol}}} = \frac{d\sigma}{d\Omega_0} \cdot \left[1 - p_\gamma^{\parallel} \Sigma \cos(2(\alpha^{\parallel} - \phi)) \right] \quad (4.3)$$

and

$$\frac{d\sigma^{\perp}}{d\Omega_{\text{pol}}} = \frac{d\sigma}{d\Omega_0} \cdot \left[1 - p_\gamma^{\perp} \Sigma \cos(2(\alpha^{\perp} - \phi)) \right] \quad (4.4)$$

$$= \frac{d\sigma}{d\Omega_0} \cdot \left[1 + p_\gamma^{\perp} \Sigma \cos(2(\alpha^{\parallel} - \phi)) \right]. \quad (4.5)$$

Note that equation (4.5) holds, because

$$\alpha^{\perp} = \alpha^{\parallel} + \pi/2 \quad \text{and} \quad \cos x = -1 \cdot \cos(x + \pi).$$

Consider now taking the difference of equations (4.3) and (4.5)

$$\frac{d\sigma^{\perp}}{d\Omega_{\text{pol}}} - \frac{d\sigma^{\parallel}}{d\Omega_{\text{pol}}} = \frac{d\sigma}{d\Omega_0} \cdot \left(p_\gamma^{\perp} + p_\gamma^{\parallel} \right) \Sigma \cos(2(\alpha^{\parallel} - \phi)). \quad (4.6)$$

One can further eliminate the unpolarized cross section from this equation by dividing by the polarization weighted sum of equations (4.3) and (4.5)

$$\alpha \cdot \frac{d\sigma^{\perp}}{d\Omega_{\text{pol}}} + \beta \cdot \frac{d\sigma^{\parallel}}{d\Omega_{\text{pol}}} = \frac{d\sigma}{d\Omega_0} \cdot \left[\alpha + \beta - \left(\alpha p_\gamma^{\perp} - \beta p_\gamma^{\parallel} \right) \Sigma \cos(2(\alpha^{\parallel} - \phi)) \right] \stackrel{!}{=} 2 \frac{d\sigma}{d\Omega_0}. \quad (4.7)$$

¹ The dependencies of polarized and unpolarized cross sections as well as the beam asymmetry like in equation (4.1) are implied

Since

$$\frac{d}{d\phi} \frac{d\sigma}{d\Omega_0} \stackrel{!}{=} 0 \forall \phi,$$

it holds

$$\alpha p_\gamma^{\parallel} - \beta p_\gamma^{\perp} \stackrel{!}{=} 0 \quad \alpha + \beta \stackrel{!}{=} 2, \quad (4.8)$$

such that

$$\alpha = \frac{2p_\gamma^{\parallel}}{p_\gamma^{\perp} + p_\gamma^{\parallel}} \quad \beta = \frac{2p_\gamma^{\perp}}{p_\gamma^{\perp} + p_\gamma^{\parallel}}. \quad (4.9)$$

The beam asymmetry Σ is thus accessible via the asymmetry

$$A(\phi) = \frac{\frac{d\sigma^{\perp}}{d\Omega \text{ pol}} - \frac{d\sigma^{\parallel}}{d\Omega \text{ pol}}}{p_\gamma^{\parallel} \frac{d\sigma^{\perp}}{d\Omega \text{ pol}} + p_\gamma^{\perp} \frac{d\sigma^{\parallel}}{d\Omega \text{ pol}}} = \Sigma \cos(2(\alpha^{\parallel} - \phi)). \quad (4.10)$$

At this point one can now make use of the fact that in any scattering reaction the number of events N is given by the product of luminosity L and total cross section σ

$$N = L \cdot \sigma = \Phi \cdot N_t \cdot \frac{d\sigma}{d\Omega} \cdot \Delta\Omega,$$

where Φ is the beam flux, N_t the number of target particles and $\Delta\Omega$ is the solid angle covered by the detector. Substituting this in equation (4.10) one can build the asymmetry $A(\phi)$ using only the (flux-)normalized event yields $\tilde{N}^{\parallel/\perp}(E_\gamma, \cos\theta, \phi)^2$

$$A(\phi) = \frac{\tilde{N}^{\perp} - \tilde{N}^{\parallel}}{p_\gamma^{\parallel} \tilde{N}^{\perp} + p_\gamma^{\perp} \tilde{N}^{\parallel}} = \Sigma \cos(2(\alpha^{\parallel} - \phi)). \quad (4.11)$$

Alternatively, the event yields N can also be normalized by integrating over the total azimuthal angle range in each bin of $(E_\gamma, \cos\theta)$. This normalization technique has been used in reference [Afz19] and will also be used in this work. Using appropriate binning in ϕ in addition to beam energy and meson polar angle the asymmetry can be build for all kinematic bins and the beam asymmetry then be extracted via a one-Parameter fit. The statistical errors for $A(\phi)$ are given by GAUSSIAN error propagation (see appendix A.1).

Frequentist

The beam asymmetry can now be determined via a frequentist fit, where Σ is determined such that the χ^2 value resulting from the data points and equation 4.11 is minimized. The results are point estimates with statistical error bars that are also obtained from the fit: $\hat{\Sigma} \pm \sigma_{\hat{\Sigma}}$. In addition $\chi^2/\text{NDF} \approx 1$ may be verified in order to diagnose the fit itself. Multiple automated minimization and calculation algorithms

² again, arguments $(E_\gamma, \cos\theta, \phi)$ are implied.

for χ^2 fitting are available as open source. The *Python* [RP22] module `scipy` [Vir+20] and *ROOT* [BR97] offer e.g. the methods `scipy.optimize.curve_fit` [sci] and `TH1::Fit()` [ROOa] for discrete/binned data, which were used in the analysis.

BAYESIAN

Following section 1.3, where the basics of BAYESIAN inference were discussed, the goal of a BAYESIAN approach is to sample marginal posterior distributions for each fitted parameter from the joint posterior $p(\theta|y)$ which depends on the observed data y . The joint posterior itself is proportional to the product of priors $\pi(\theta)$ and likelihood $\mathcal{L}(y|\theta)$ (BAYES’ theorem). This collapses to a one parameter problem in the case of fitting the event yield asymmetries (Eq. (4.11))

$$p(\Sigma|y) \propto \pi(\Sigma) \cdot \mathcal{L}(y|\Sigma). \quad (4.12)$$

However, to be able to sample from a joint posterior, prior and likelihood need to be specified. In order not to bias the fit towards any particular values, the prior is chosen non-informative, realized by a broad GAUSSIAN centered at 0 which is truncated to the physically allowed parameter space of $\Sigma \in [-1, 1]$. Furthermore, the likelihood is formulated assuming GAUSSIAN errors ϵ_n at each data point y_n , which should be described by the asymmetry (Eq (4.11)) at bin n $A(\phi_n; \Sigma)$, i. e.³

$$\Sigma \sim \mathcal{N}(0, 1)_{[-1, 1]} \quad y_n = A(\phi_n; \Sigma) + \epsilon_n \quad \epsilon_n \sim \mathcal{N}(0, \sigma_n), \quad (4.13)$$

which is equivalent to

$$\Sigma \sim \mathcal{N}(0, 1) \quad y_n \sim \mathcal{N}(A(\phi_n; \Sigma), \sigma_n). \quad (4.14)$$

The likelihood of all data points now evaluates to the product of the likelihood at each data point y_n and the posterior results in

$$p(\Sigma|y) \propto \pi(\Sigma) \cdot \mathcal{L}(y|\Sigma) = \mathcal{N}(\Sigma|0, 1)_{[-1, 1]} \cdot \prod_n \mathcal{N}(y_n|A(\phi_n; \Sigma), \sigma_n) \quad (4.15)$$

$$\Leftrightarrow -\ln p(\Sigma|y) = \frac{1}{2}\Sigma^2 + \frac{1}{2} \sum_n \left(\frac{y_n - A(\phi_n; \Sigma)}{\sigma_n} \right)^2 + \text{constant terms}, \quad (4.16)$$

such that all ingredients are present to form a fully BAYESIAN probabilistic model⁴. This model was implemented in Stan [Sta22], directly giving access to samples from the posterior obtained with the No-U-Turn-Sampler (NUTS) [Sta22; HG14]. Hereby, the sampling is restricted to the allowed parameter region $\Sigma \in [-1, 1]$. As a measure of goodness of fit, the p -values obtained from the posterior predictive distributions, as introduced in section 1.3, are reviewed. To diagnose the convergence of the MCMC fit, sensible values for \hat{R} and the Monte-Carlo standard error σ_{MCSE} are verified.

³ Remember the notation introduced in section 1.3: $x \sim \mathcal{N}(\mu, \sigma) = \mathcal{N}(x|\mu, \sigma) = \frac{1}{\sqrt{2\pi\sigma^2}} e^{-\frac{(x-\mu)^2}{2\sigma^2}}$

⁴ Note that the sampling aims only to reflect the right proportionality of the (marginal) posterior. Thus, constant terms can be dropped and are of no further interest [Sta22].

4.1.2 Event based fit

Although intuitive and easily implementable the binned fit –BAYESIAN or not– has one critical disadvantage: it is inevitable that information is lost because the asymmetry $A(\phi)$ is a binned quantity and hence, the choice of binning influences the fit results. This is discussed in more detail in appendix B. Especially kinematic bins with low statistics show this behavior. To circumvent this problem, an *unbinned fit*, based on the likelihood function for each event, can be performed. Also, no assumptions on the distribution of statistical errors have to be made since each event is taken into account individually. Yet, the event based fit does not provide any measure of goodness of fit, so that the study of toy Monte Carlo data is essential when checking the working principle of the method.

In a polarized experiment the azimuthal angle distribution of events is not isotropic, but modulated by a cosine term coupling to beam asymmetry Σ and beam polarization $p_\gamma^{\parallel/\perp}$ for each setting $\alpha^{\parallel/\perp}$, as is expressed through the respective differential cross sections in Equations 4.3 and 4.4. Since the number of events is proportional to the cross section, the probability $p(\phi, p_\gamma^{\parallel/\perp} | \Sigma)$ to find an event under the azimuthal angle ϕ for a given bin of $(E_\gamma, \cos \theta)$ and setting $\alpha^{\parallel/\perp}$ is⁵

$$p(\phi, p_\gamma^{\parallel/\perp} | \Sigma) = \frac{[1 \mp p_\gamma^{\parallel/\perp} \Sigma \cos(2(\alpha^\parallel - \phi))]}{\frac{1}{2\pi} \int_0^{2\pi} d\phi [1 \mp p_\gamma^{\parallel/\perp} \Sigma \cos(2(\alpha^\parallel - \phi))]} \quad (4.17)$$

This is only true for an idealized experiment with acceptance $\epsilon = \text{const} \forall \phi$, so that the acceptance $\epsilon(\phi)$ has to be included in the probability for each event. As demonstrated in reference [Har17] a FOURIER series truncated after the fourth order is sufficient to model any occurring function

$$\epsilon(\phi) = \sum_{k=0}^4 a_k \sin(k\phi) + b_k \cos(k\phi),$$

where the eight detector coefficients a_k and b_k are determined from the fit. With this the measurable probability $\tilde{p}(\phi, p_\gamma^{\parallel/\perp} | \Sigma, a, b)$ is

$$\tilde{p}(\phi, p_\gamma^{\parallel/\perp} | \Sigma, a, b) \propto [1 \mp p_\gamma^{\parallel/\perp} \Sigma \cos(2(\alpha^\parallel - \phi))] \cdot \epsilon(\phi) \quad (4.18)$$

$$= [1 \mp p_\gamma^{\parallel/\perp} \Sigma \cos(2(\alpha^\parallel - \phi))] \cdot \left(\sum_{k=0}^4 a_k \sin(k\phi) + b_k \cos(k\phi) \right), \quad (4.19)$$

where $a := \{a_k\}_{k=0}^4$, $b := \{b_k\}_{k=0}^4$. Finally, normalizing $\frac{1}{2\pi} \int_0^{2\pi} d\phi \tilde{p}(\phi, p_\gamma^{\parallel/\perp} | \Sigma, a, b) \stackrel{!}{=} 1$,

$$\tilde{p}(\phi, p_\gamma^{\parallel/\perp} | \Sigma, a, b) = \frac{[1 \mp p_\gamma^{\parallel/\perp} \Sigma \cos(2(\alpha^\parallel - \phi))] \cdot \left(\sum_{k=0}^4 a_k \sin(k\phi) + b_k \cos(k\phi) \right)}{1 \pm \frac{1}{2} a_2 p_\gamma^{\parallel/\perp} \Sigma}. \quad (4.20)$$

⁵ Note: Normalizing $p(\phi, p_\gamma^{\parallel/\perp} | \Sigma)$ to 2π (or any other arbitrary constant) is sufficient for the fit as long as the integral does not depend on the fit parameters. The normalization to 2π is chosen for better readability. However, to calculate actual probabilities, one must multiply Eq. (4.17) by 2π .

The respective polarization setting $\alpha^{\parallel/\perp}$ determines the sign in the normalizing constant which allows an uncorrelated estimation of the detector coefficient a_2 and the beam asymmetry Σ . To simplify notation and implementation, Equation (4.21) can be written as *one* probability for all events – regardless of polarization setting – if the polarization values p_γ^\parallel are multiplied by (-1) and summarized as p_γ :

$$\tilde{p}(\phi, p_\gamma | \Sigma, a, b) = \frac{[1 + p_\gamma \Sigma \cos(2(\alpha - \phi))] \cdot (\sum_{k=0}^4 a_k \sin(k\phi) + b_k \cos(k\phi))}{1 - \frac{1}{2}a_2 p_\gamma \Sigma}, \quad (4.21)$$

with $\alpha = -45^\circ$ fixed.

In section 3.2 the subtraction of uncorrelated time background was discussed via a sideband subtraction. Naturally, without binning the data, this strategy is invalid and prompt peak and sideband events have to be fitted simultaneously. Hereby it is important to consider that the random time background is realized as flat distribution underneath the complete reaction time spectrum (cf. Figure 3.3), *including* the range of the prompt peak. The fraction of true coincident events to random coincidences is given as

$$f = \frac{N_{\text{prompt}} - w \cdot N_{\text{sideband}}}{N_{\text{prompt}}}, \quad (4.22)$$

where N_{prompt} and N_{sideband} are the number of events where the reaction time lies within the prompt peak or sideband, respectively. w is the ratio of the widths of the chosen prompt peak and sideband ranges, see section 3.2. It is now assumed that the random coincidences will exhibit an asymmetry Σ^{bkg} of their own and are not necessarily described by the detector coefficients a and b but rather by a^{bkg} and b^{bkg} . The probability to detect a prompt peak event p_{prompt} and the probability to measure a sideband event p_{sideband} are then given by

$$p_{\text{prompt}}(\phi, p_\gamma | \Sigma, a, b, \Sigma^{\text{bkg}}, a^{\text{bkg}}, b^{\text{bkg}}) = f \cdot \tilde{p}(\phi, p_\gamma | \Sigma, a, b) + (1 - f) \cdot \tilde{p}(\phi, p_\gamma | \Sigma^{\text{bkg}}, a^{\text{bkg}}, b^{\text{bkg}}) \quad (4.23)$$

$$p_{\text{sideband}}(\phi, p_\gamma | \Sigma^{\text{bkg}}, a^{\text{bkg}}, b^{\text{bkg}}) = \tilde{p}(\phi, p_\gamma | \Sigma^{\text{bkg}}, a^{\text{bkg}}, b^{\text{bkg}}). \quad (4.24)$$

If there are n prompt peak and m sideband events, the joint likelihood of all events \mathcal{L} is thus given by

$$\mathcal{L} = \prod_{i=1}^n p_{\text{prompt}}(\phi_i, p_{\gamma,i} | \Sigma, a, b, \Sigma^{\text{bkg}}, a^{\text{bkg}}, b^{\text{bkg}}) \prod_{j=1}^m p_{\text{sideband}}(\phi_j, p_{\gamma,j} | \Sigma, a, b, \Sigma^{\text{bkg}}, a^{\text{bkg}}, b^{\text{bkg}}), \quad (4.25)$$

or, equivalently

$$\begin{aligned} \ln \mathcal{L} &= \sum_{i=1}^n \ln p_{\text{prompt}}(\phi_i, p_{\gamma,i} | \Sigma, a, b, \Sigma^{\text{bkg}}, a^{\text{bkg}}, b^{\text{bkg}}) \\ &\quad + \sum_{j=1}^m \ln p_{\text{sideband}}(\phi_j, p_{\gamma,j} | \Sigma, a, b, \Sigma^{\text{bkg}}, a^{\text{bkg}}, b^{\text{bkg}}). \end{aligned} \quad (4.26)$$

Eighteen⁶ parameters have to be determined in total, either via a conventional frequentist approach or a BAYESIAN approach to this non-linear fitting problem.

Frequentist

Best fit estimates can be derived by maximizing the likelihood \mathcal{L} , or, for computational convenience, by minimizing $-\ln \mathcal{L}$. The *ROOT* library [BR97] offers the method *TTree::UnbinnedFit* to perform an unbinned maximum likelihood fit on data filled in a *TTree* [ROOb], which was used to perform the fit. Minimization and statistical error calculation are performed by *MINUIT* [JR75]. Errors are hereby estimated either symmetrical from the paraboloid shape of $(-\ln \mathcal{L})$ using the *HESSE* algorithm or asymmetric from the half-maximum values of $(-\ln \mathcal{L})$ using the *MINOS* algorithm without making assumptions on the shape of the likelihood, if necessary [JR75].

Bayesian

The joint posterior of all fit parameters given the data ϕ, p_γ is

$$p(\Sigma, a, b, \Sigma^{\text{bkg}}, a^{\text{bkg}}, b^{\text{bkg}} | \phi, p_\gamma) \propto \mathcal{L}(\phi, p_\gamma | \Sigma, a, b, \Sigma^{\text{bkg}}, a^{\text{bkg}}, b^{\text{bkg}}) \cdot \pi(\Sigma, a, b, \Sigma^{\text{bkg}}, a^{\text{bkg}}, b^{\text{bkg}}), \quad (4.27)$$

where $\pi(\theta)$ denotes the combined prior of all fit parameters which factors into each individual prior since all parameters are independent:

$$\pi(\Sigma, a, b, \Sigma^{\text{bkg}}, a^{\text{bkg}}, b^{\text{bkg}}) = \pi(\Sigma) \cdot \pi(a) \cdot \pi(b) \cdot \pi(\Sigma^{\text{bkg}}) \cdot \pi(a^{\text{bkg}}) \cdot \pi(b^{\text{bkg}}). \quad (4.28)$$

The priors for $\Xi \in \{\Sigma, \Sigma^{\text{bkg}}\}$ and $\xi \in \{a, b, a^{\text{bkg}}, b^{\text{bkg}}\}$ are again chosen non-informative, broadly centered around 0

$$\Xi \sim \mathcal{N}(0, 1)_{[-1, 1]} \quad \xi_k \sim \mathcal{N}(0, 0.1). \quad (4.29)$$

This model, consisting of the likelihood in Eq. (4.26) and the priors in Eq. (4.29), is implemented in Stan [Sta22], so that samples from the posterior in the physically allowed region ($\Xi \in [-1, 1]$) are again obtained via NUTS [HG14]. From references [Afz19; Har17] it is expected that $\xi_k \ll 1$, therefore the chosen widths of the priors resemble a, relatively speaking, broad distribution.

4.2 Determination of Σ_η using Bayesian statistics

This section will now demonstrate the application of the discussed methods to obtain the beam asymmetry Σ for η photoproduction with selected data provided from reference [Afz19]. For each method only the respective BAYESIAN approach will be used and compared to the results from [Afz19] to confirm that it is a valid method. As an additional sanity check toy Monte Carlo samples are generated and analyzed.

⁶ The FOURIER series is constructed such that $a_0 = 0, b_0 = 1$

4.2.1 Application of methods to toy Monte Carlo data

Although results can be compared to the already accomplished ones in reference [Afz19], verifying the correct functioning of the fitting methods is still useful. This is done by generating events that follow the expected distributions of $N^{\parallel/\perp}$ with fixed and known parameters. With the simulated event yields the binned and unbinned fit are performed as described previously. Repeating this for a large number of times should reproduce the input parameters if the methods work as intended.

Event yield asymmetries

The asymmetry $A(\phi)$ is built from the event yields $N^{\parallel/\perp}$, which are distributed according to

$$N^{\parallel} = N_0 \left[1 - p_{\gamma}^{\parallel} \Sigma \cos(2(\alpha^{\parallel} - \phi)) \right], \quad (4.30)$$

$$N^{\perp} = N_0 \left[1 - p_{\gamma}^{\perp} \Sigma \cos(2(\alpha^{\perp} - \phi)) \right], \quad (4.31)$$

where the parameters are chosen as $\Sigma = 0.3$, $p_{\gamma}^{\parallel} = 0.25$, $p_{\gamma}^{\perp} = 0.3$. In each toy Monte Carlo bin the number of generated samples per setting $N_{\text{total}}^{\parallel/\perp}$ is given by a Poisson distribution

$$N_{\text{total}}^{\parallel} \sim \mathcal{P}(800) \quad N_{\text{total}}^{\perp} \sim \mathcal{P}(1000), \quad (4.32)$$

to simulate the statistics of the $\gamma p \rightarrow p\eta$ final state as accurately as possible [Afz19]. The samples from the distributions (4.30),(4.31) are drawn using the *TH1::GetRandom* [ROOc] function provided by *ROOT* [BR97]. The function from which samples should be drawn is integrated point wise and then normalized. The normalized integral is approximated by a parabola for each bin. A random number between 0 and 1 is generated and assigned to the according bin, where the respective parabola is evaluated to give the desired random value. [ROOc]. In total, 10000 toy Monte Carlo bins were simulated and the asymmetry built for 12 bins in ϕ , to conform with the binning chosen in reference [Afz19]. The resulting asymmetry $A(\phi)$ is shown in Figure 4.2 for several bins as the orange data points with statistical errors according to GAUSSIAN error propagation. Additionally shown is a χ^2 fit (orange line) to the asymmetry together with posterior predictive checks as obtained from a fully BAYESIAN fit according to the introduced model (blue distributions). This BAYESIAN fit was performed employing $n_{\text{chain}} = 4$ MARKOV chains with $n_{\text{samples}} = 1000$ samples each. The warm-up period for each chain has the same length of $n_{\text{warm up}} = 1000$

$$n_{\text{chain}} = 4 \quad n_{\text{samples}} = 1000 \quad n_{\text{warm up}} = 1000. \quad (4.33)$$

The goodness of fit is checked via the introduced p -values $p = T(A_{\text{rep}} > A)$, and are shown as black points with propagated error bars on the bottom. The optimal value of $p = 0.5$ is marked by the dashed line and realizes the mean of the distribution of all p -values, so that one can assume good description of the data by the fits, see Figure 4.3. This replaces the investigation of the χ^2/NDF distribution in the case of a frequentist fit, which should have a mean of 1.

4.2 Determination of Σ_η using Bayesian statistics

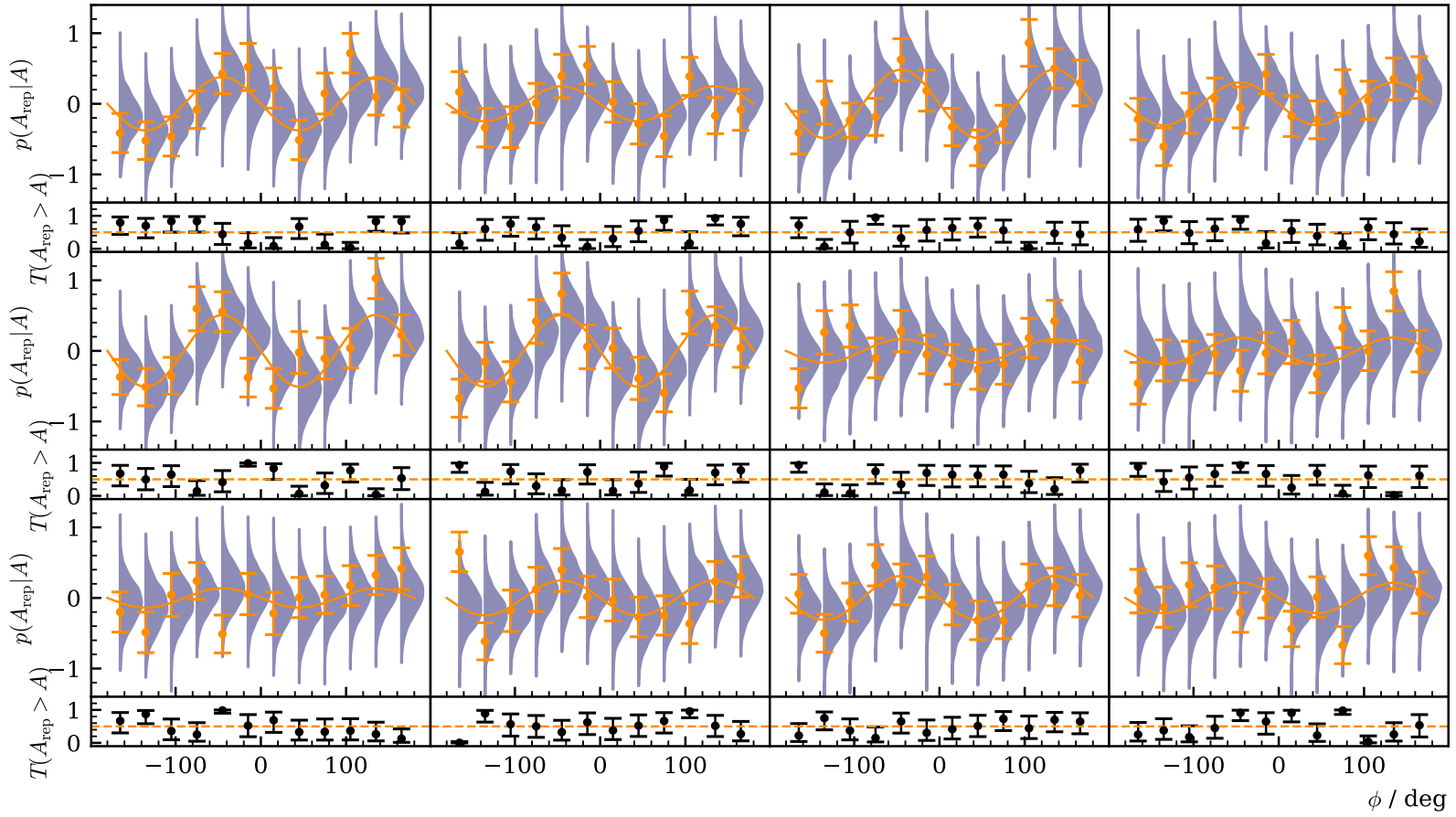


Figure 4.2: Posterior predictive checks $p(A_{\text{rep}}|A)$ from a BAYESIAN fit to the event yield asymmetries for six toy Monte Carlo bins are shown as distributions. The data points in the upper plot are the asymmetry $A(\phi)$, which was additionally fitted using a χ^2 fit (solid line). The goodness of fit is shown using p -values, which give the fraction $T(A_{\text{rep}} > A)$ of replicated samples greater than the original measured value, with propagated statistical error bars on the bottom of each plot. The expected mean value of $T(A_{\text{rep}} > A) = 0.5$ is indicated by the dashed line.

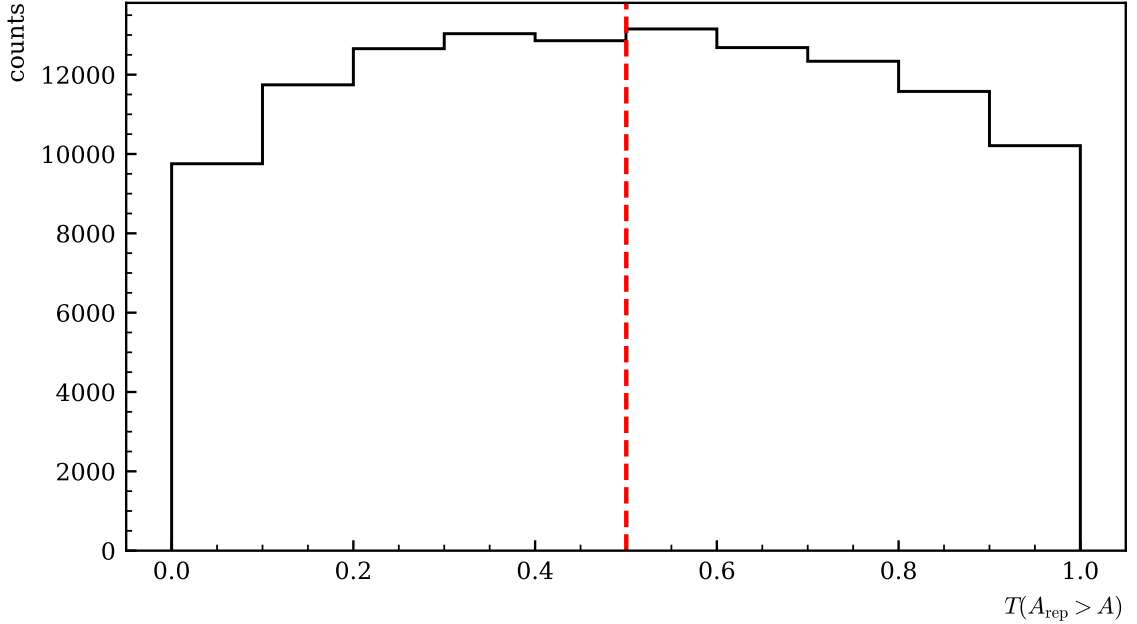


Figure 4.3: p values of all toy Monte Carlo bins. They are centered around their mean at 0.5, which is indicated by the dashed line, and show no bias towards higher or lower values, thus confirming an adequate fit.

To check whether the fit is unbiased and provides correct error estimation one can investigate the normalized residuals

$$\xi = \frac{\Sigma^{\text{fit}} - \Sigma^{\text{true}}}{\Delta\Sigma^{\text{fit}}} \quad (4.34)$$

in the case of a least-squares fit. Here Σ^{fit} and $\Delta\Sigma^{\text{fit}}$ are the value and corresponding statistical error for the beam asymmetry as obtained from the fit and Σ^{true} is the true value that was used to throw the toy MC experiments. An unbiased fit with right estimation of errors yields [Bar89]

$$\xi \sim \mathcal{N}(0, 1). \quad (4.35)$$

This criterion obviously cannot be applied in the same way to a BAYESIAN fit. The fit results are distributions and therefore lack point estimates Σ^{fit} and errors $\Delta\Sigma^{\text{fit}}$. However, one can modify Equation (4.34) to the needs of a BAYESIAN fit to assess its performance:

$$\Xi = \frac{\{\Sigma^{\text{fit}}\} - \Sigma^{\text{true}}}{\text{std}(\{\Sigma^{\text{fit}}\})} \sim \mathcal{N}(0, \sigma). \quad (4.36)$$

Instead of the point estimates Σ^{fit} the set of all draws from the marginal posteriors $\{\Sigma^{\text{fit}}\}$ is shifted by the true value Σ^{true} and normalized by the standard deviation as an error estimate for each fit. Although this is not a rigorously derived quantity it allows to identify possible bias if $\text{mean}(\Xi) \neq 0$. Furthermore, checking that $\sigma \approx 1$ will affirm whether the width of the marginal posterior distributions

is sensible. Figure 4.4 shows the combined Ξ -distributions of all fits and the unaltered combined posteriors shifted by the true value. As expected, both distributions are normal as a GAUSSIAN fit proves. The width of the marginal posterior distributions can be regarded as sensible since the

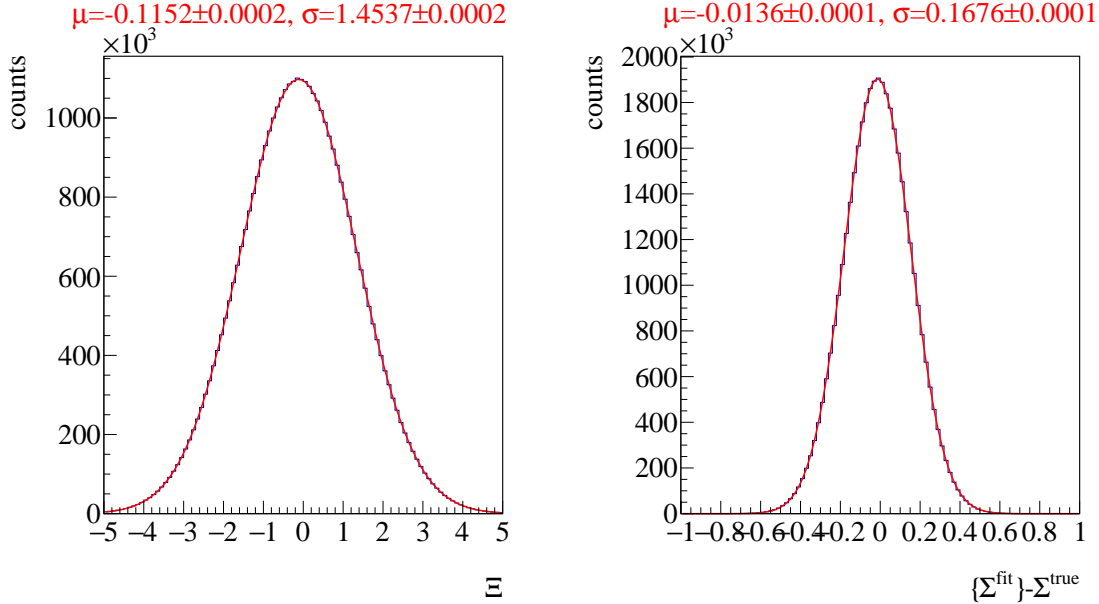


Figure 4.4: Left: Combined posterior distributions of all 10000 fits normalized by their respective standard deviation. Right: Unaltered combined posterior distributions of all 10000 fits. A GAUSSIAN fit was performed to determine mean μ and standard deviation σ of the distributions with results given on top.

standard deviation of the Ξ distribution $\sigma_\Xi \approx 1^7$. This is furthermore confirmed by the fact that $\{\Sigma^{\text{fit}}\} - \Sigma^{\text{true}} = 0$ within one standard deviation. Yet, the fit results tend to underestimate the beam asymmetry, because both distributions are centered out of their statistical error at $\mu \pm \Delta\mu < 0$. This indicates bias towards smaller values of the beam asymmetry. Remarkably, this bias is *not* introduced by the BAYESIAN fit, but by the choice of binning and available statistics as an extensive investigation of binned fits (least squares and BAYESIAN) to toy Monte Carlo data showed. A detailed discussion thereof is given in appendix B. For now it suffices to note the origin of this bias lies in the choice of binning and is thus inevitable. And, most importantly, the introduced bias is negligible compared to the width of the posterior distributions, so that a binned fit will produce valid fit results in any case. Nevertheless this emphasizes the advantage of unbinned fitting, which is discussed in the next paragraph.

It has been established that the fit produces valid results with sensible statistical errors, i.e. widths of posterior distributions, and the description of the data is in agreement with the expectations. It remains to diagnose the convergence of the MARKOV chains to finally deem the binned fit method appropriate. For this the \hat{R} value and the relative Monte Carlo standard error (MCSE) $\frac{\sigma_{\text{MCSE}}}{\text{median}[\rho(\Sigma|y)]}$ that were introduced in section 1.3 are investigated. If $\hat{R} < 1.05$ one can assume that the different chains have converged and explored the same parameter space [Veh+19]. Furthermore the accuracy

⁷ One cannot expect to fulfill Eq. (4.35) exactly, since the errors are after all only estimates that aim to create comparability to the least squares fit.

supplied by the number of draws from the posteriors can be evaluated with the relative MCSE. It is demanded that $\frac{\sigma_{\text{MCSE}}}{\text{median}[p(\Sigma|y)]} \lesssim 5\%$. This is the case for 97% of all fits, see Figure 4.5 on the left. When the fit result for the beam asymmetry is close to 0 larger values for the relative MCSE are observed. The \hat{R} values (Figure 4.5 on the right) clearly indicate good within and between chain convergence. This means that the hyper parameters n_{chain} , n_{samples} and $n_{\text{warm up}}$ as chosen are well tuned, although one may increase the number of sample draws from the posterior for the fit from measured data to further suppress the relative MCSE. Then, only $11 \cdot 12$ as opposed to 10000 fits have to be performed keeping the computational cost reasonable.

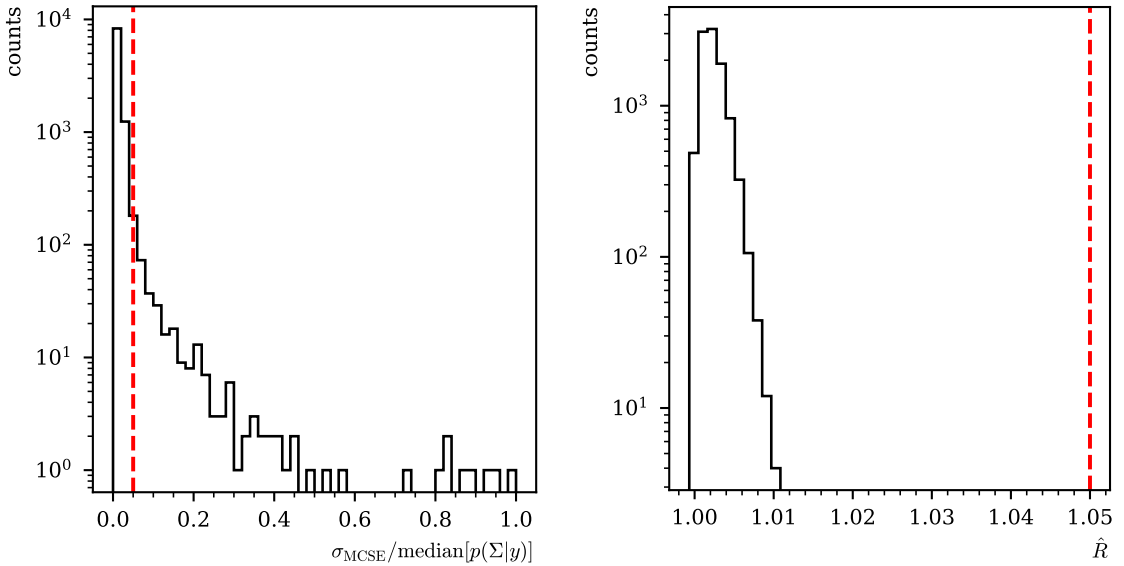


Figure 4.5: Left: relative error $\frac{\sigma_{\text{MCSE}}}{\text{median}[p(\Sigma|y)]}$ Right: \hat{R} associated with the fit parameter Σ . Both are shown for all 10000 fits. The critical values that should not be exceeded are marked by dashed lines.

Event based fit

Not only signal events but also contributions from random time background as well as the imperfect detector efficiency $\epsilon(\phi)$ have to be simulated in order to test the method of event based fitting. For each polarization setting prompt peak and sideband events are drawn from the theoretical ϕ -distributions p_{prompt} and p_{sideband} which are given in Equations (4.23) and (4.24). The total number of draws per setting and bin is again given by Poisson distributions and the ratio of prompt peak to sideband events is given by the time cut weights $\{w_i\}_{i=1}^7$ employed for the actual analysis of the $p\eta$ final state data [Afz19]. This means that seven times prompt peak and sideband events need to be simulated. The fraction of background events within the prompt peak f was set to $f = 0.95$. Further, the values $p_\gamma^\parallel = 0.25$, $p_\gamma^\perp = 0.3$, $\Sigma = 0.5$, $\Sigma^{\text{bkg}} = -0.5$ and lastly, a random efficiency function as already chosen in reference [Afz19] were appointed. Finally the hyperparameters n_{chain} , n_{samples} , $n_{\text{warm up}}$ are chosen the same as previously. Table 4.1 shows a summary of all toy Monte Carlo properties. In total, 1000 toy Monte Carlo experiments are thrown. To evaluate the fit results only the posterior distributions are available. As before, the residuals Ξ are built from all fits, now for Σ as well as Σ^{bkg} . They are

chosen parameters	$p_\gamma^{\parallel} = 0.25, p_\gamma^{\perp} = 0.3, \Sigma = 0.5, \Sigma^{\text{bkg}} = -0.5, f = 0.95,$ $w_1 = \frac{15}{210}, w_2 = \frac{8}{210}, w_3 = \frac{4}{210}, w_4 = \frac{10}{210}, w_5 = \frac{14}{210}, w_6 = \frac{6}{210}, w_7 = \frac{11}{210}$
simulation draws	$7 \cdot N_{\text{total},i}^{\parallel} \sim \mathcal{P}(800), 7 \cdot N_{\text{total},i}^{\perp} \sim \mathcal{P}(1000) \quad _{i=1}^7$
	signal in prompt background in prompt sideband
	$N_{\text{total}}^{\parallel/\perp} \cdot f$ $N_{\text{total}}^{\parallel/\perp} \cdot (1-f)$ $N_{\text{total}}^{\parallel/\perp} \cdot (1-f) \cdot 1/w_i$
efficiency function	$\epsilon(\phi) = 1/10.5 \cdot (9.3 + 0.28 \cdot \cos \phi + 0.24 \cdot \sin 3\phi)$
hyperparameters	$n_{\text{samples}} = 1000, n_{\text{chain}} = 4, n_{\text{warm up}} = 1000$

Table 4.1: Summary of the complete setting of all toy Monte Carlo experiments for the event based fit. Values and table layout adapted from [Afz19].

shown in Figure 4.6 together with the unnormalized posterior distributions. Note that the distributions are truncated towards the tails at $\Sigma \rightarrow 1$ and $\Sigma^{\text{bkg}} \rightarrow -1$ as implemented in the BAYESIAN fit in Stan. Also the event based fit is able to reproduce the true values within one standard deviation. Only slight bias towards smaller values of the beam asymmetry is seen, but again with negligible effect on the results in comparison to the widths of the distributions. If the total amount of posterior distributions is not too large one might also combine them in a *pooled likelihood* approach (see subsection ??). This is shown in Figure 4.7 for both determined asymmetries. Because the true asymmetries are within 1σ of the resulting distribution one can finally conclude that the event based fit estimates positions and widths of the posterior distributions correctly.

A check of the relative MCSE and \widehat{R} values as shown in Figure 4.8 reveals also that the hyperparameters $n_{\text{chain}}, n_{\text{samples}}, n_{\text{warm up}}$ are correctly tuned. It is noteworthy that the event based fit creates more precise results although less Monte Carlo experiments in total were performed than for the binned fit.

Next to signal and background beam asymmetry the fit also estimates an efficiency function $\epsilon(\phi)$ that is described by a FOURIER series. The polarization weighted sum of event yields allows to confirm whether a good description of the efficiency is achieved because it is given by the efficiency function modulated only by a constant, see previous section 4.1 $\alpha \tilde{N}^{\parallel} + \beta \tilde{N}^{\perp} = c \cdot \epsilon(\phi)$. Figure 4.9 shows the weighted sum of event yields with the same binning as used in the binned fit together with a posterior predictive check using the draws of all parameters distributions a, b . As opposed to the binned fit it is not only performed at each data point but for significantly more points. This mimics a continuous function as is appropriate for an unbinned fit. However, for better visibility the posterior predictive distributions are not built at every point but the efficiency function is plotted for each set of draws $a^{(s)}, b^{(s)}, s = 1 \dots 4000$. No p values are estimated since they would not be representative of the whole fit. The mean of the posterior predictive distributions is given by the dashed line and agrees within statistical error bars with the simulated data.

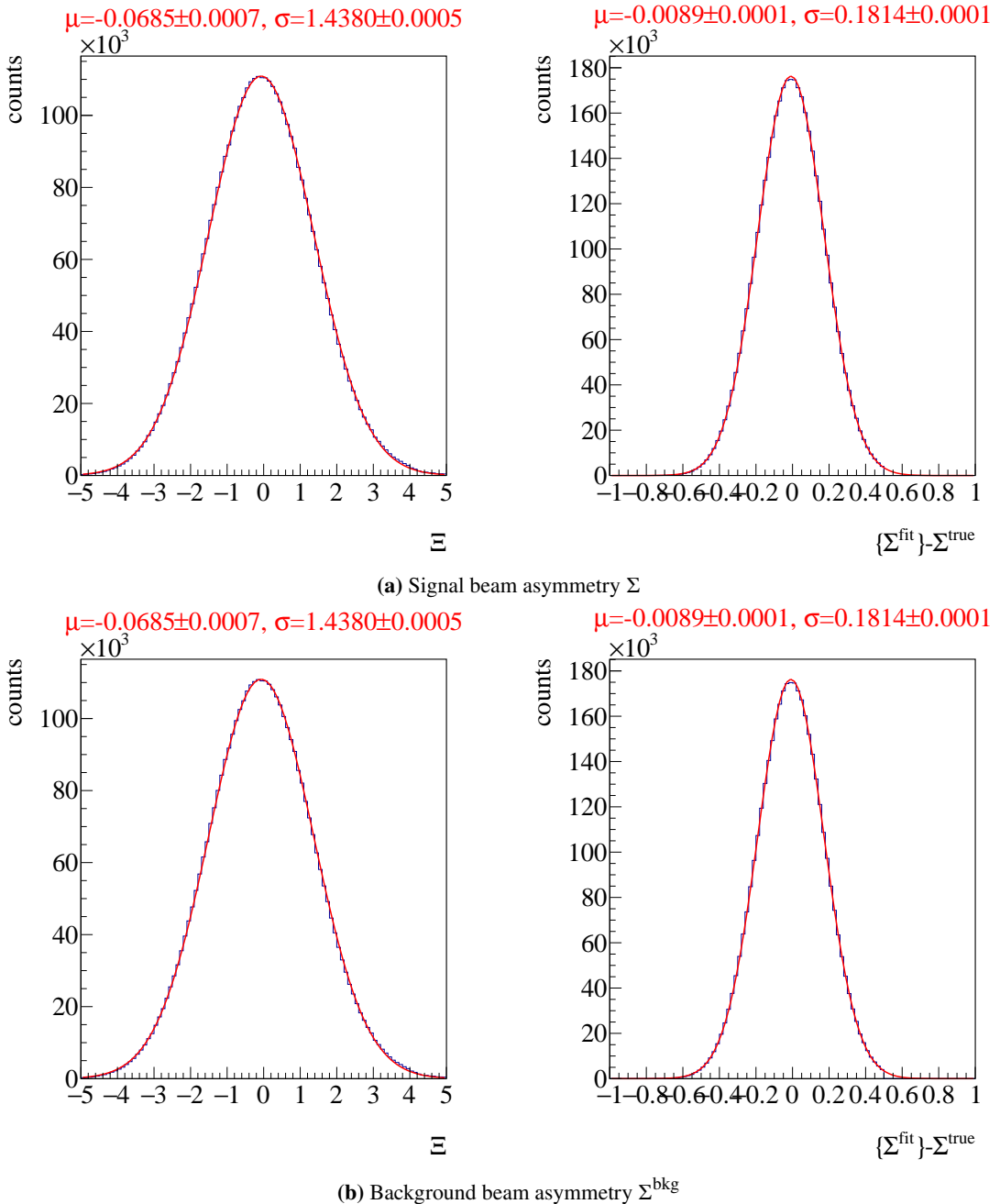


Figure 4.6: Combined posteriors for the beam asymmetries Σ and Σ^{bkg} from all 1000 event based fits. Left: Residuals Ξ Right: Unnormalized posterior distributions. A GAUSSIAN fit is performed on the distributions with results for mean μ and standard deviation σ on top.

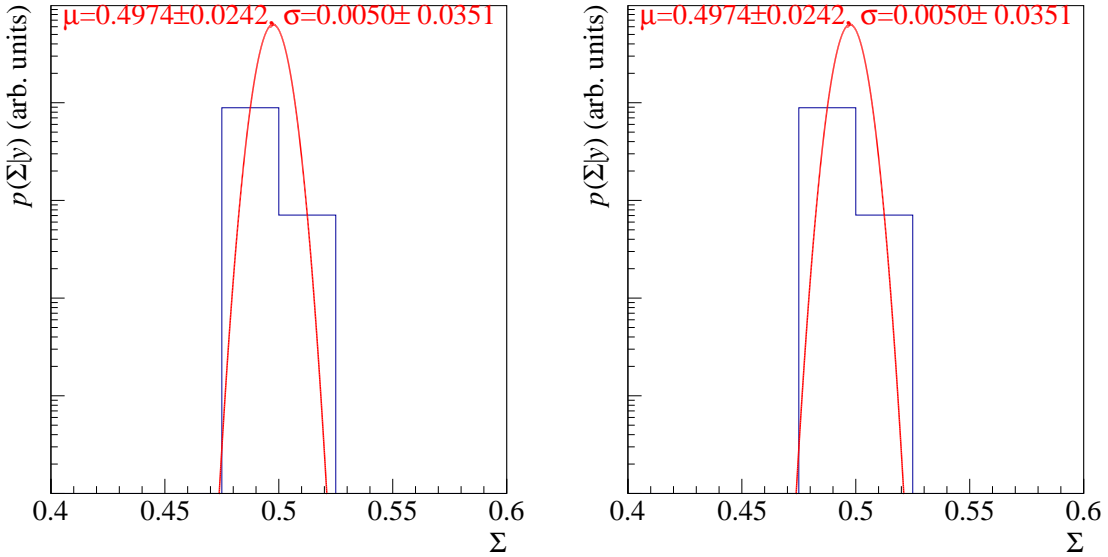


Figure 4.7: Combined posterior probabilities using the *pooled likelihood* approach. Left: Signal beam asymmetry, Right: background beam asymmetry. Mean and standard deviation as obtained from a Gaussian fit are shown on top

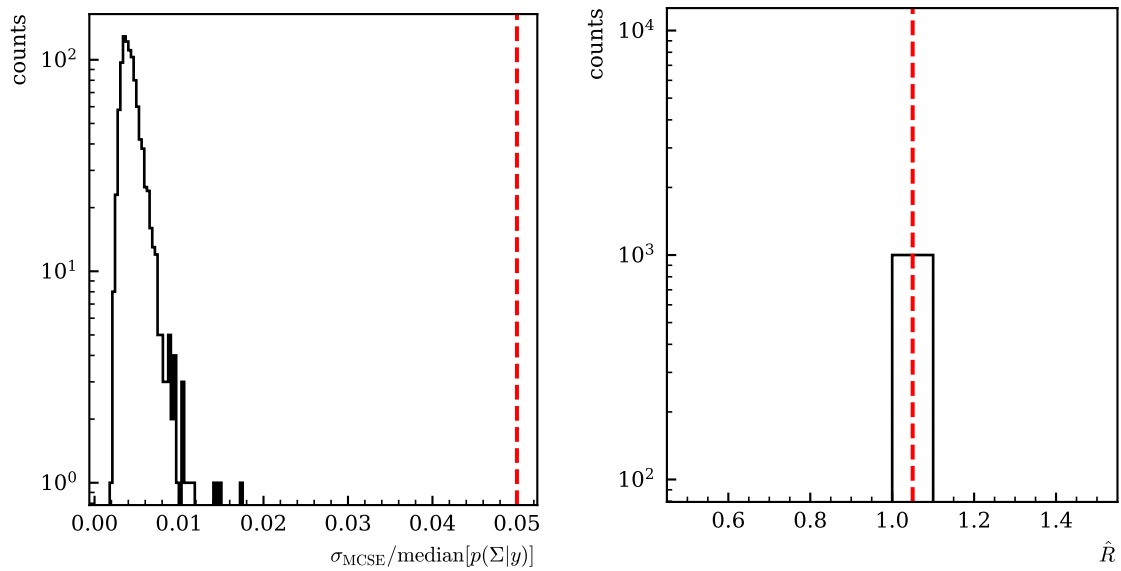


Figure 4.8: Left: relative error $\frac{\sigma_{\text{MCSE}}}{\text{median}[p(\Sigma|y)]}$. Right: \hat{R} associated with the fit parameter Σ . Both are shown for all 1000 fits. The critical values that should not be exceeded are marked by dashed lines.

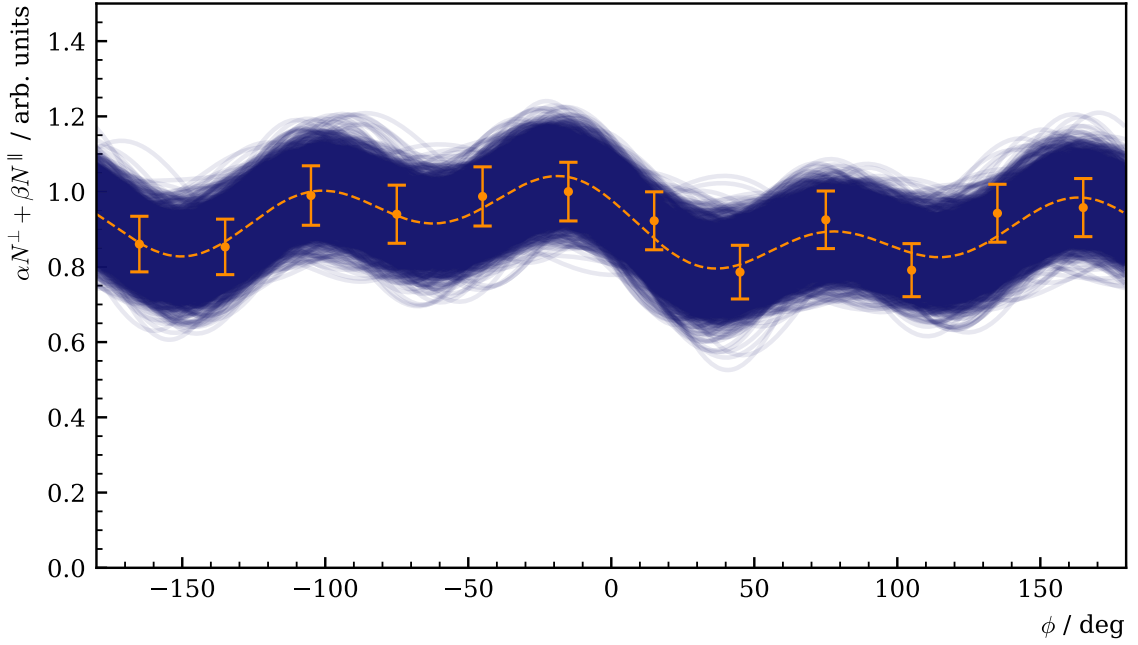


Figure 4.9: Posterior predictive check using the draws of the detector coefficients a and b . Points with error bars are the polarization weighted sum of event yields. The dashed line is the mean of the predictive values while the solid opaque lines are representative of one simulation draw $a^{(s)}, b^{(s)}$.

4.2.2 Application of methods to data

Since both methods were tested successfully using toy Monte Carlo data, both are subsequently applied to real data to extract the beam asymmetry. Since the number of fits is small compared to the amount of fits performed during testing, the amount of posterior draws was increased to 5000 per chain. All other hyperparameters were left the same

$$n_{\text{samples}} = 5000 \quad n_{\text{chain}} = 4 \quad n_{\text{warm up}} = 1000. \quad (4.37)$$

Event yield asymmetries

In all bins of beam energy and meson polar angle the binned fit was performed. Similar to the Monte Carlo samples, 12 bins in phi are built to comply with the binning in reference [Afz19], and guarantee comparability.

Figure 4.10 shows the resulting asymmetry $A(\phi)$ for all angular bins for the energy bin $1250 \text{ MeV} \leq E_\gamma < 1310 \text{ MeV}$ as orange data points with statistical error bars. Additionally shown is a χ^2 fit (orange line) to the asymmetry together with posterior predictive checks as obtained from a fully BAYESIAN fit according to the introduced model (blue distributions). The goodness of fit is checked via the introduced p -values $p = T(A_{\text{rep}} > A)$, and are shown as black points with propagated error bars on the bottom. The optimal value of $p = 0.5$ is marked by the dashed line and realizes the mean of the distribution of all p -values, so that one can assume good description of the data by the fits, see Figure 4.11. This replaces the investigation of the χ^2/NDF distribution in the case of a frequentist fit.

4.2 Determination of Σ_η using Bayesian statistics

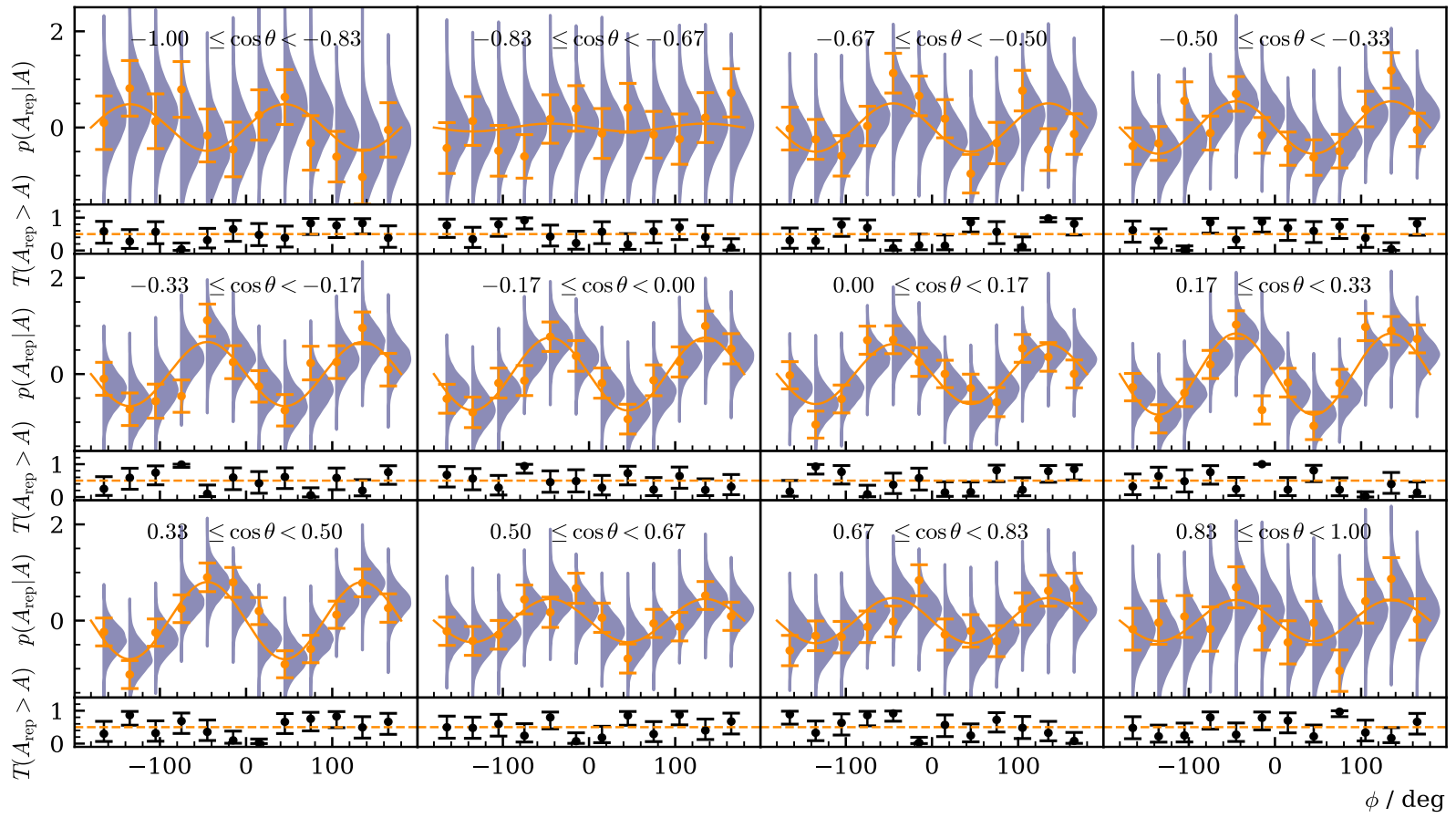


Figure 4.10: Posterior predictive checks $p(A_{\text{rep}}|A)$ from a BAYESIAN fit to the event yield asymmetries for all angular bins of the energy bin $1250 \text{ MeV} \leq E_\gamma < 1310 \text{ MeV}$. The data points in the upper plot are the asymmetry $A(\phi)$, which was additionally fitted using a χ^2 fit (solid line). The goodness of fit is shown using p -values, which give the fraction $T(A_{\text{rep}} > A)$ of replicated samples greater than the original measured value, with propagated statistical error bars on the bottom of each plot. The expected mean value of $T(A_{\text{rep}} > A) = 0.5$ is indicated by the dashed line.

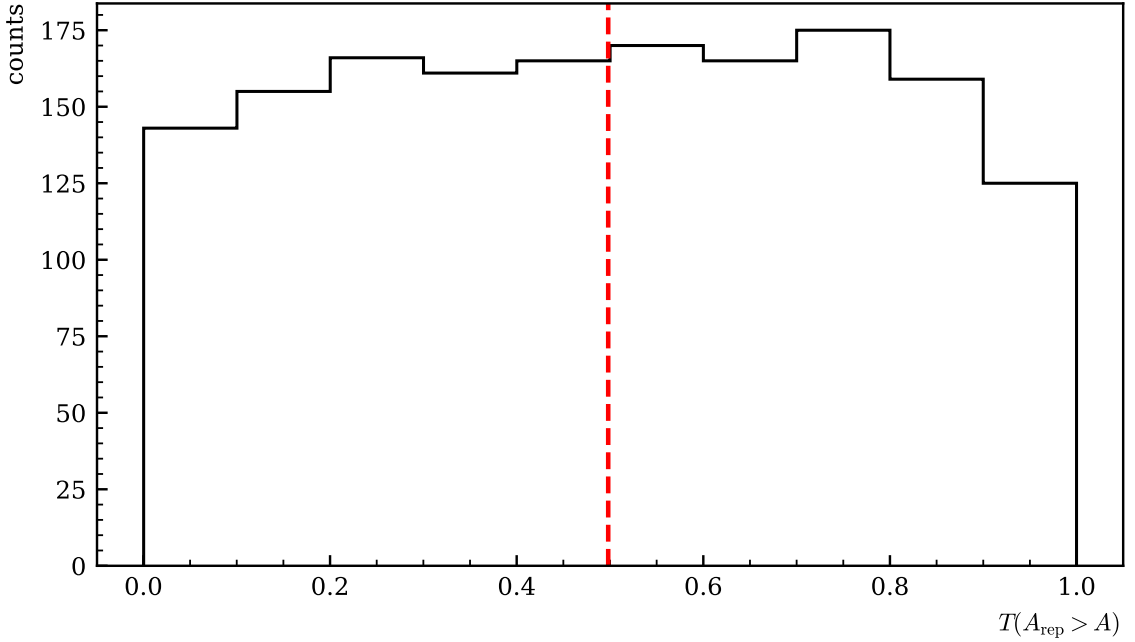


Figure 4.11: p values generated using all fits. They are centered around their mean at 0.5, which is indicated by the dashed line, and show no bias towards higher or lower values, thus confirming an adequate fit.

The MCMC diagnostics reveal that all MARKOV chains have converged and explored the available parameter space completely which is characterized by $\widehat{R} = 1.00$ for all fits. The increment of posterior draws removed any fluctuations in the \widehat{R} value that was present before. The relative MCSE is below the (self-)defined threshold of $\frac{\sigma_{\text{MCSE}}}{\text{median}[P(\Sigma|y)]} < 5\%$ for 95% of all fits. The remaining 5% are fits that estimated the beam asymmetry close to 0 such that further incrementing the number of posterior draws will not amend this. Both, relative MCSE and \widehat{R} associated with the fit parameter Σ of the binned fit, are shown in Figure 4.12. Thus, one can conclude the successful tuning of hyperparameters concerning the BAYESIAN fit.

Event based fit

The discussed BAYESIAN event based fit is also performed for all kinematic bins. The MCMC diagnostics reveal good choice of hyperparameters, as Figure 4.13 shows. As already observed during the toy Monte Carlo experiments, the unbinned fit produces more precise results; 98% of all fits exhibit an MCSE below threshold, those bins with error above threshold are again explained by values of the beam asymmetry $\Sigma \approx 0$. Good within and between chain convergence is reached, as $\widehat{R} = 1.00$ for all fits shows.

The only illustrative measure regarding the performance of the unbinned fit is the posterior predictive distribution of the detector coefficients a, b . Figure 4.14 shows the weighted sum of event yields with the same binning as used in the binned fit together with a posterior predictive check using the draws of all parameters distributions a, b for the kinematic bin $1250 \text{ MeV} \leq E_\gamma < 1310 \text{ MeV}, 0 \leq \cos \theta < 0.17$. As opposed to the binned fit it is not only performed at each data point but for significantly more points. This mimics a continuous function as is appropriate for an unbinned fit. However, for better

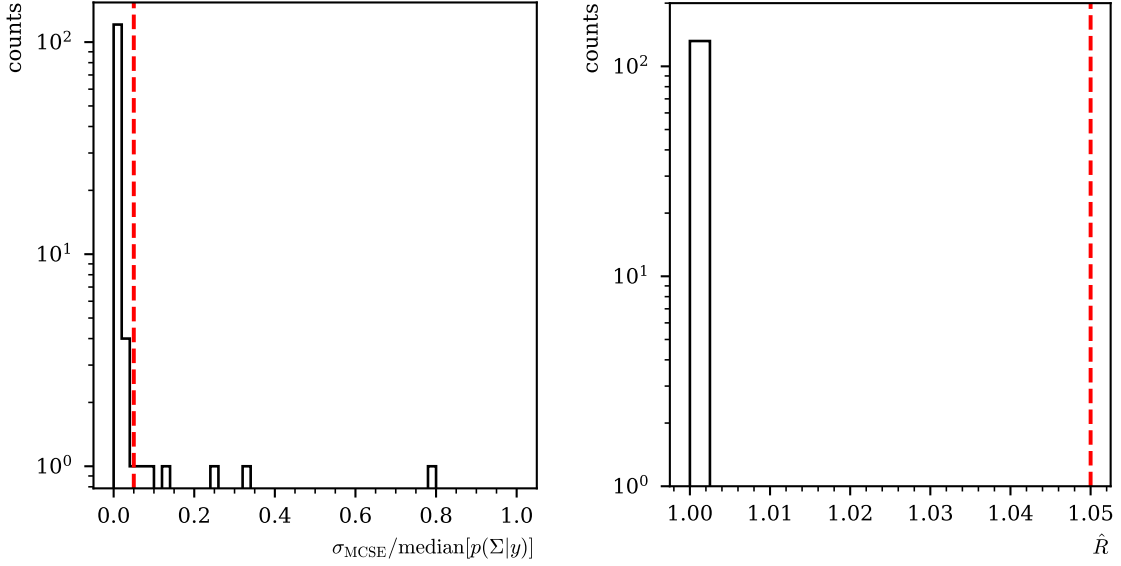


Figure 4.12: Left: relative error $\frac{\sigma_{\text{MCSE}}}{\text{median}[p(\Sigma|y)]}$ Right: \hat{R} associated with the fit parameter Σ . Both are shown for all $11 \cdot 12$ binned fits to the asymmetry $A(\phi)$. The critical values that should not be exceeded are marked by dashed lines.

visibility the posterior predictive distributions are not built at every point but the efficiency function is plotted for each set of draws $a^{(s)}, b^{(s)}, s = 1 \dots 20000$. No p values are estimated since they would not be representative of the whole fit. Note that the detector efficiency $\epsilon(\phi)$ is almost flat as opposed to the simulated efficiency in subsection 4.2.1. This is an overall observation and not specific to the shown kinematic bin and further confirmed by the fact that the sums of all fit coefficients a, b are distributed around zero. Regardless of the significance of detection inefficiencies the unbinned fit is nevertheless able to obtain good agreement between fit and data; the mean of all posterior predictive distributions (dashed line) agrees within statistical error bars with the data points.

4.2.3 Discussion

The final results for the beam asymmetry obtained with both methods are shown in Figure 4.15 for all bins in beam energy and meson polar angle. Along with the marginal posterior distributions obtained from both introduced methods point estimates from a χ^2 fit and an unbinned fit [Afz19] are shown. An important intermediate result is that all results agree with each other within statistical error bars or within the width of the marginal posterior distributions. Any effects that lead to slightly distinguishable point estimates from a binned or unbinned fit are propagated directly throughout the BAYESIAN fit; then each distribution is centered around the point estimate of the respective fitting method. Thus, in general, the application of BAYESIAN methods has proven to give the same results and no systematic error is introduced by the BAYESIAN approach.

The effort of implementing the binned or unbinned fit in a BAYESIAN approach is comparable to using standard libraries provided by e.g. *python* [RP22] or *ROOT* [BR97]. Due to the probabilistic structure of the Stan language [Sta22] implementation of likelihood and prior models is straightforward

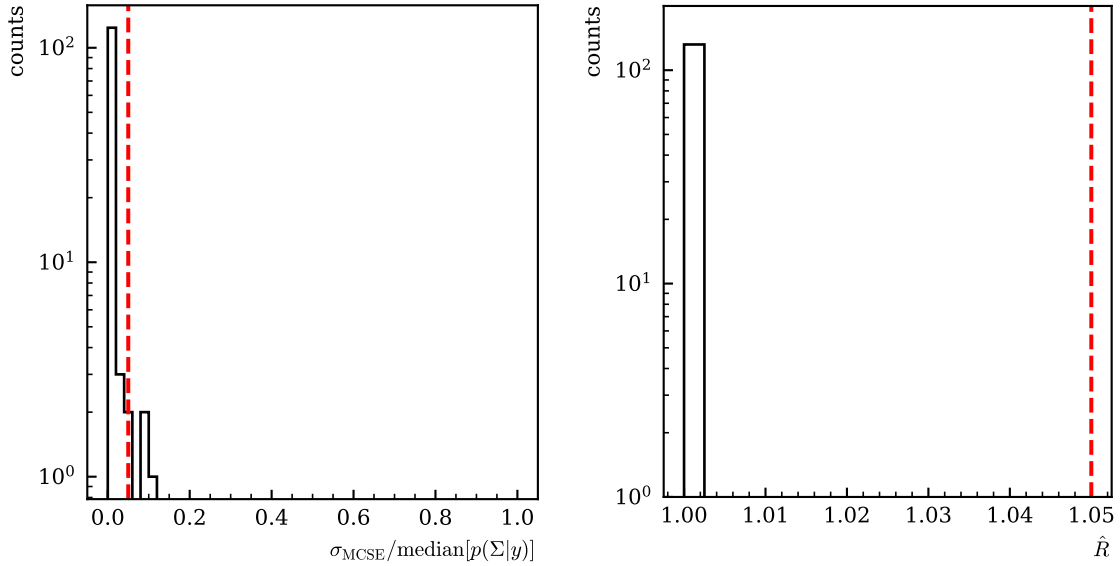


Figure 4.13: Left: relative error $\frac{\sigma_{\text{MCSE}}}{\text{median}[p(\Sigma|y)]}$. Right: \hat{R} associated with the fit parameter Σ . Both are shown for all fits. The critical values that should not be exceeded are marked by dashed lines.

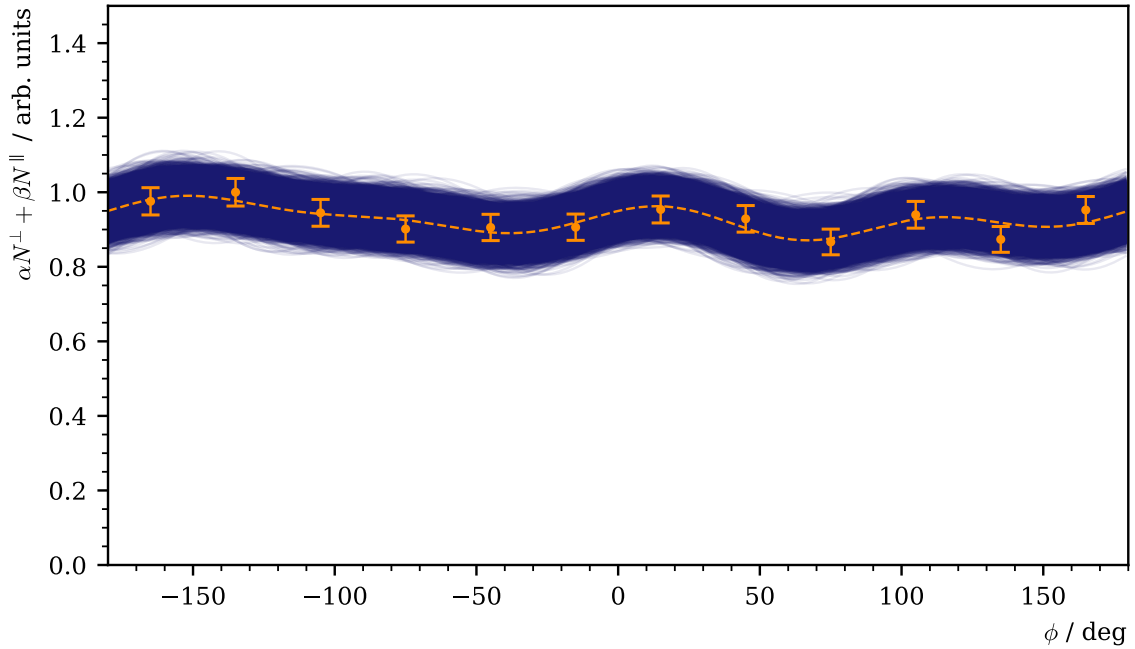


Figure 4.14: Posterior predictive check using the draws of the detector coefficients a and b for the kinematic bin $1250 \text{ MeV} \leq E_\gamma < 1310 \text{ MeV}, 0 \leq \cos \theta < 0.17$. Points with error bars are the polarization weighted sum of event yields. The dashed line is the mean of the predictive values while the solid opaque lines are representative of one simulation draw $a^{(s)}, b^{(s)}$.

and the sampling algorithms can be accessed or modified to ones needs intuitively. However, the BAYESIAN fit requires more careful preparation and also diagnostics. On one hand, the choice of priors has to be made. On the other hand, the fitting procedure is inherently different; not only the goodness of fit compared with data has to be checked but also the convergence of the MARKOV chains themselves.

The computational cost also increases greatly in comparison to the traditional frequentist approaches. Especially the unbinned BAYESIAN fit requires a lot of computation time, where the number of data points is of order $O(10^4)$ as opposed to 12 data points for the binned fit. This can be understood considering the underlying algorithms; the least squares fit and also the unbinned maximum likelihood fit both aim to minimize a given test statistic which is achievable by (numeric) differentiation. Determining marginal posterior distributions from BAYESIAN inference on the other hand requires (numeric) integration, making it the more complex task which is observable in the consumed computation time.

Yet, the additional effort is rewarded by the fact that the BAYESIAN fit will yield *distributions* for all parameters as opposed to point estimates with error bars. This is especially useful for polarization observables which may be used as input for PWA calculations. Here error estimates can be derived from the distributions e.g. as (multiple) standard deviations, the full width at half maximum or similar. If furthermore a BAYESIAN approach is pursued, also the whole distributions may be used. Another advantage of the BAYESIAN fit is the ability to truncate the posterior samples to the relevant or allowed parameter space. In the very first energy bin in Figure 4.15 this is visible clearly where several point estimates exceed the physical limit of $\Sigma = 1$ as opposed to the obtained marginal posteriors. Lastly, the BAYESIAN fit allows much more flexible changes to the fitted model, as will be discussed in the next section 4.3.

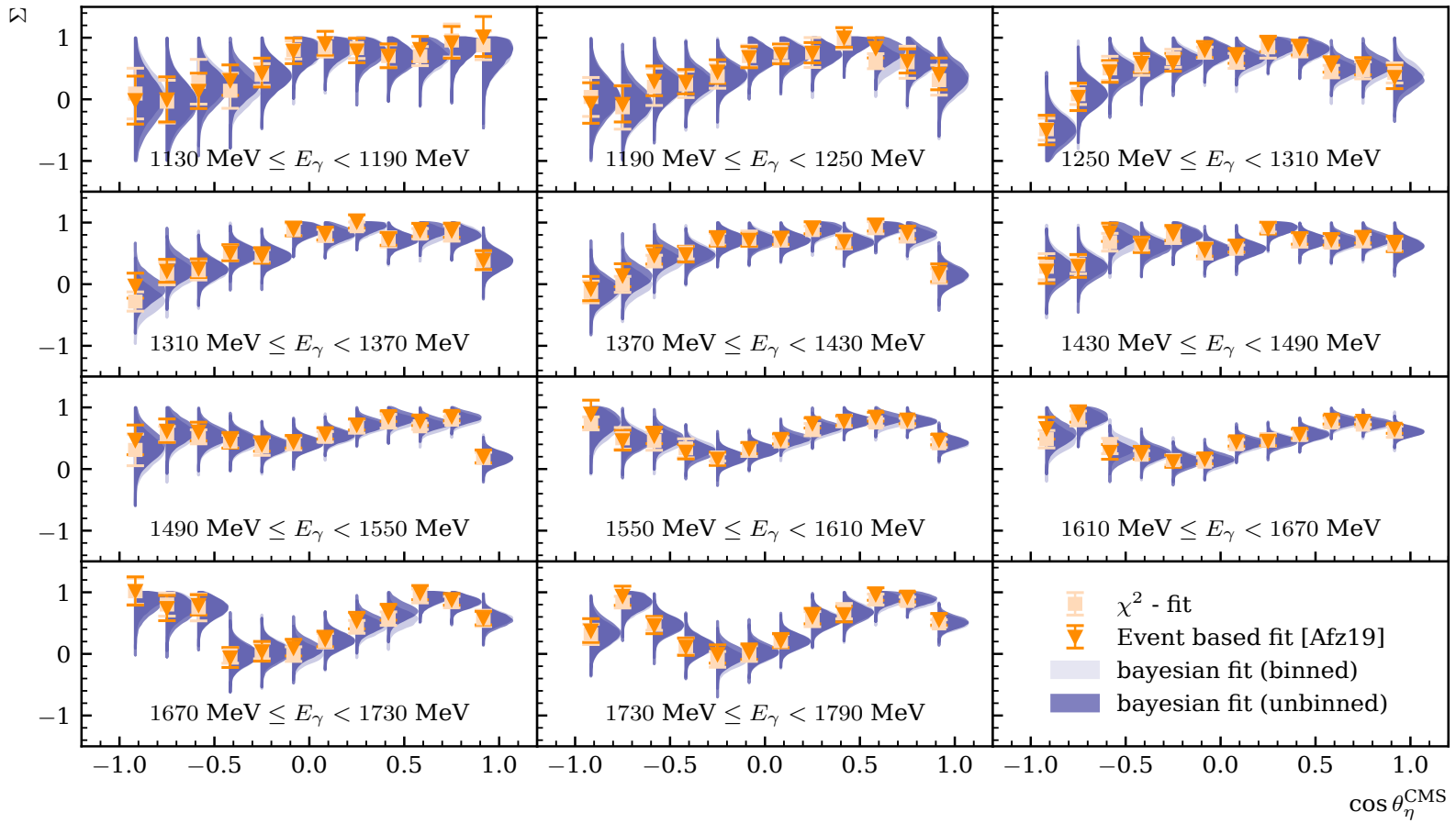


Figure 4.15: Final results for the beam asymmetry Σ in η photoproduction off the proton for all kinematic bins obtained with BAYESIAN methods. They are compared with the results of a least squares fit and an unbinned fit as given in reference [Afz19]. All results agree within statistical error bars or within the widths of marginal posterior distributions.

4.3 Determination of $\Sigma_{\eta'}$

4.3.1 Application of event based fit to toy Monte Carlo data

placeholder

4.3.2 Application of event based fit to data

placeholder

4.3.3 Systematic Error

placeholder

Bibliography

- [Zyl+20] P. Zyla et al., *Review of Particle Physics*, PTEP **2020** (2020) 083C01.
- [LMP01] U. Löring, B. Metsch and H. Petry, *The light-baryon spectrum in a relativistic quark model with instanton-induced quark forces*, The European Physical Journal A **10** (2001) 395, ISSN: 1434-601X, URL: <http://dx.doi.org/10.1007/s100500170105>.
- [KS03] B. Krusche and S. Schadmand, *Study of nonstrange baryon resonances with meson photoproduction*, Prog. Part. Nucl. Phys. **51** (2003) 399, arXiv: nucl-ex/0306023.
- [Afz19] F. N. Afzal, *Measurement of the beam and helicity asymmetries in the reactions $\gamma p \rightarrow p\pi^0$ and $\gamma p \rightarrow p\eta$* , PhD thesis: Rheinische Friedrich-Wilhelms-Universität Bonn, 2019, URL: <https://hdl.handle.net/20.500.11811/8064> (cit. on pp. 34, 35, 39, 40, 44, 45, 48, 51, 54).
- [DT92] D. Drechsel and L. Tiator, *Threshold pion photoproduction on nucleons*, J. Phys. G **18** (1992) 449.
- [Bar+18] M. Bartelmann et al., *Theoretische Physik 3 — Quantenmechanik*, 2018, ISBN: 978-3-662-56071-6.
- [Bar89] R. J. Barlow, *Statistics, A Guide to the Use of Statistical Methods in the Physical Sciences*, Wiley, 1989 (cit. on p. 42).
- [Wal] D. Walther, *Crystal Barrel, A 4π photon spectrometer*, URL: <https://www.cb.uni-bonn.de> (visited on 27/09/2021).
- [Urb17] M. Urban, *Design eines neuen Lichtpulsersystems sowie Aufbau und Inbetriebnahme der neuen APD Auslese für das Crystal-Barrel-Kalorimeter*, PhD thesis: Rheinische Friedrich-Wilhelms-Universität Bonn, 2017.
- [Afz22] F. Afzal, *Private communication*, 2022.
- [Ike+00] H. Ikeda et al., *A detailed test of the CsI(Tl) calorimeter for BELLE with photon beams of energy between 20-MeV and 5.4-GeV*, Nucl. Instrum. Meth. A **441** (2000) 401.
- [Har17] J. Hartmann, *Measurement of Double Polarization Observables in the Reactions $\gamma p \rightarrow p\pi^0$ and $\gamma p \rightarrow p\eta$ with the Crystal Barrel/TAPS Experiment at ELSA*, Rheinische Friedrich-Wilhelms-Universität Bonn, 2017, URL: <https://hdl.handle.net/20.500.11811/7258> (cit. on pp. 37, 39).
- [Cre+09] V. Crede et al., *Photoproduction of eta and eta-prime mesons off protons*, Phys. Rev. C **80** (2009) 055202, arXiv: 0909.1248 [nucl-ex].

Bibliography

- [Die+20] M. Dieterle et al.,
Helicity-Dependent Cross Sections for the Photoproduction of π^0 Pairs from Nucleons,
Physical Review Letters **125** (2020),
URL: <https://doi.org/10.1103/physrevlett.125.062001>.
- [Käs+18] A. Käser et al., *First measurement of helicity-dependent cross sections in $\pi^0\eta$ photoproduction from quasi-free nucleons*, Physics Letters B **786** (2018) 305,
URL: <https://doi.org/10.1016/j.physletb.2018.10.006>.
- [San+11] A. M. Sandorfi, S. Hoblit, H. Kamano and T.-S. H. Lee,
Determining pseudoscalar meson photoproduction amplitudes from complete experiments,
Journal of Physics G: Nuclear and Particle Physics **38** (2011) 053001, ISSN: 1361-6471,
URL: <http://dx.doi.org/10.1088/0954-3899/38/5/053001> (cit. on p. 33).
- [Afz+20] F. Afzal et al.,
Observation of the $p\eta'$ Cusp in the New Precise Beam Asymmetry Σ Data for $\gamma p \rightarrow p\eta$,
Phys. Rev. Lett. **125** (15 2020) 152002,
URL: <https://link.aps.org/doi/10.1103/PhysRevLett.125.152002>
(cit. on p. 34).
- [RP22] G. van Rossum and the Python development team,
The Python Language Reference, Release 3.10.5, 2022,
URL: <https://docs.python.org/3.10/reference/index.html>
(cit. on pp. 36, 51).
- [Vir+20] P. Virtanen et al., *SciPy 1.0: Fundamental Algorithms for Scientific Computing in Python*,
Nature Methods **17** (2020) 261 (cit. on p. 36).
- [BR97] R. Brun and F. Rademakers, *ROOT — An object oriented data analysis framework*,
Nucl. Instrum. Meth. A **389** (1997) 81, ISSN: 0168-9002, URL: <https://www.sciencedirect.com/science/article/pii/S016890029700048X>
(cit. on pp. 36, 39, 40, 51).
- [sci] scipy, *scipy.optimize.curve_fit, Function Documentation*,
URL: https://docs.scipy.org/doc/scipy/reference/generated/scipy.optimize.curve_fit.html (visited on 28/06/2022) (cit. on p. 36).
- [ROOa] ROOT, *TH1 Class reference*, URL: <https://root.cern.ch/doc/master/classTH1.html#a63eb028df86bc86c8e20c989eb23fb2a> (visited on 28/06/2022) (cit. on p. 36).
- [Sta22] Stan development team, *Stan Modeling Language Users Guide and Reference Manual*,
vol. 2.29, 2022, URL: <https://mc-stan.org> (cit. on pp. 36, 39, 51).
- [HG14] M. D. Hoffman and A. Gelman,
The No-U-Turn Sampler: Adaptively Setting Path Lengths in Hamiltonian Monte Carlo,
Journal of Machine Learning Research **15** (2014) 1593,
URL: <http://jmlr.org/papers/v15/hoffman14a.html> (cit. on pp. 36, 39).
- [ROOb] ROOT, *TTree Class reference*, URL: <https://root.cern.ch/doc/master/classTTree.html#a3e6bf252ab8653b47cc9116950f3ee7b> (visited on 28/06/2022)
(cit. on p. 39).

-
- [JR75] F. James and M. Roos, *Minuit - a system for function minimization and analysis of the parameter errors and correlations*, Computer Physics Communications **10** (1975) 343, ISSN: 0010-4655, URL:
<https://www.sciencedirect.com/science/article/pii/0010465575900399> (cit. on p. 39).
 - [ROOc] ROOT, *TF1 Class reference*, URL: <https://root.cern.ch/doc/master/classTF1.html#a410b0219e18e80d3e305b4d97374c077> (visited on 28/06/2022) (cit. on p. 40).
 - [Veh+19] A. Vehtari, A. Gelman, D. Simpson, B. Carpenter and P.-C. Bürkner, *Rank-normalization, folding, and localization: An improved \hat{R} for assessing convergence of MCMC*, arXiv e-prints, arXiv:1903.08008 (2019) arXiv:1903.08008, arXiv: 1903.08008 [stat.CO] (cit. on p. 43).

List of Figures

1.1	Running coupling of QCD. The colored data points represent different methods to obtain a value for α_s . For more details it may be referred to [Zyl+20].	2
1.2	Calculated nucleon (isospin $I = 1/2$) resonances compared to measurements. Left in each column are the calculations [LMP01], the middle shows the measurements and PDG rating [Zyl+20]	3
1.3	FEYNMAN diagram for the s-channel photoproduction of pseudoscalar mesons, adapted from [Afz19]	4
2.1	[Wal]	7
2.2	[Wal]	8
2.3	[Wal]	8
2.4	D. WALTHER in [Urb17]	9
2.5	[Wal]	9
2.6	[Wal]	10
3.1	Distribution of event classes in $\eta' \rightarrow \gamma\gamma$ production	12
3.2	Time information of all final state particles and the beam photon for 3PED η' production	13
3.3	Reaction time t_r for 3PED η' production	14
3.4	Coplanarity of the $p\eta'$ final state with all other cuts applied for the energy bin $1\,500\,\text{MeV} \leq E_\gamma < 1\,600\,\text{MeV}$. The vertical dashed lines show the cut ranges obtained from a gaussian fit to the data (open circles). The solid black histograms represent fitted MC data of $\eta' \rightarrow \gamma\gamma$	18
3.5	Polar angle difference of the $p\eta'$ final state with all other cuts applied for the energy bin $1\,500\,\text{MeV} \leq E_\gamma < 1\,600\,\text{MeV}$. The vertical dashed lines show the cut ranges obtained from a gaussian fit to the data (open circles). The solid black histograms represent fitted MC data of $\eta' \rightarrow \gamma\gamma$	18
3.6	Missing mass of the $p\eta'$ final state with all other cuts applied for the energy bin $1\,500\,\text{MeV} \leq E_\gamma < 1\,600\,\text{MeV}$. The vertical dashed lines show the cut ranges obtained from a fit to data (open circles) employing a Novosibirsk function. The solid colored histograms represent fitted MC data from relevant photoproduction reactions: in black η' , in green π^0 , in red η , in blue ω , in yellow $2\pi^0$, magenta $\pi^0\eta$. The turquoise histogram is the sum of all MC histograms.	19

3.7	Invariant mass of the $p\eta'$ final state with all other cuts applied for all energy and angular bins. The open circles represent the measured data, the solid colored histograms fitted MC data from relevant photoproduction reactions: in black η' , in green π^0 , in red η , in blue ω , in yellow $2\pi^0$ and in magenta $\pi^0\eta$. The turquoise histogram is the sum of all MC histograms.	20
3.8	Invariant mass of the $p\eta'$ final state with all other cuts applied for the energy bin $1500 \text{ MeV} \leq E_\gamma < 1600 \text{ MeV}$. The vertical dashed lines show the cut ranges obtained from a gaussian fit to the η' MC data (solid black histogram). The open circles represent the measured data, the solid colored histograms fitted MC data from relevant photoproduction reactions: in black η' , in green π^0 , in red η , in blue ω , in yellow $2\pi^0$ and in magenta $\pi^0\eta$. The turquoise histogram is the sum of all MC histograms.	21
3.9	Acceptance for the reaction $\gamma p \rightarrow p\eta'$ after all cuts that have been discussed so far for 2.5PED and 3PED events	22
3.10	Fraction of background events in the analyzed beam energy and angular bins.	23
3.11	Acceptance for possible background contributions	24
3.12	Generated energies of the two lowest energy photons in $2\pi^0$ photoproduction MC data. The threshold of 20 MeV is marked by a vertical red line. Lowest energy photon is shown on the top, second lowest energy photon is shown on the bottom.	25
3.13	Generated energies of the two lowest energy photons in $2\pi^0$ and $\pi^0\eta$ photoproduction MC data. The threshold of 20 MeV is marked by a vertical red line. Lowest energy photon is shown on the top, second lowest energy photon is shown on the bottom.	26
3.14	Polar angle difference $\Delta\theta$ between the photon with second highest energy and second lowest energy of the $\pi^0\eta$ final state.	26
3.15	Illustration of the misidentification process during reconstruction	27
3.16	Generated CMS angle $\cos\theta_{\text{gen.}}$ vs. reconstructed CMS angle $\cos\theta_{\text{rec.}}$ for both background reactions. The slope $\cos\theta_{\text{gen.}} = \cos\theta_{\text{rec.}}$ is indicated by the solid line.	28
3.17	Detector hits of the recoil proton, as obtained from MC data for the production of η' , $2\pi^0$ and $\pi^0\eta$. CB: Crystal Barrel, FW: forward detector, MT: MiniTAPS	30
3.18	Difference in measured and calculated beam energy. Data points are shown as open circles, MC data as solid histograms: in black η' , in green π^0 , in red η , in blue ω , in yellow $2\pi^0$ and in magenta $\pi^0\eta$. The turquoise histogram is the sum of all MC histograms.	31
3.19	Invariant mass spectrum passing different stages in the event selection process. In the end clear peaks for all possibly produced mesons are visible. The vertical lines indicate the mean cut ranges over all energy and angle bins.	32
4.1	Left: Definition of angles α, ϕ, φ . Right: Photon momentum \vec{k} and polarization $\vec{\epsilon}$ define the beam polarization plane while the reaction plane is defined by the recoil proton p and produced meson M	33

4.2 Posterior predictive checks $p(A_{\text{rep}} A)$ from a BAYESIAN fit to the event yield asymmetries for six toy Monte Carlo bins are shown as distributions. The data points in the upper plot are the asymmetry $A(\phi)$, which was additionally fitted using a χ^2 fit (solid line). The goodness of fit is shown using p -values, which give the fraction $T(A_{\text{rep}} > A)$ of replicated samples greater than the original measured value, with propagated statistical error bars on the bottom of each plot. The expected mean value of $T(A_{\text{rep}} > A) = 0.5$ is indicated by the dashed line.	41
4.3 p values of all toy Monte Carlo bins. They are centered around their mean at 0.5, which is indicated by the dashed line, and show no bias towards higher or lower values, thus confirming an adequate fit.	42
4.4 Left: Combined posterior distributions of all 10000 fits normalized by their respective standard deviation. Right: Unaltered combined posterior distributions of all 10000 fits. A GAUSSIAN fit was performed to determine mean μ and standard deviation σ of the distributions with results given on top.	43
4.5 Left: relative error $\frac{\sigma_{\text{MCSE}}}{\text{median}[p(\Sigma y)]}$ Right: \widehat{R} associated with the fit parameter Σ . Both are shown for all 10000 fits. The critical values that should not be exceeded are marked by dashed lines.	44
4.6 Combined posteriors for the beam asymmetries Σ and Σ^{bkg} from all 1000 event based fits. Left: Residuals Ξ Right: Unnormalized posterior distributions. A GAUSSIAN fit is performed on the distributions with results for mean μ and standard deviation σ on top.	46
4.7 Combined posterior probabilities using the <i>pooled likelihood</i> approach. Left: Signal beam asymmetry, Right: background beam asymmetry. Mean and standard deviation as obtained from a Gaussian fit are shown on top	47
4.8 Left: relative error $\frac{\sigma_{\text{MCSE}}}{\text{median}[p(\Sigma y)]}$ Right: \widehat{R} associated with the fit parameter Σ . Both are shown for all 1000 fits. The critical values that should not be exceeded are marked by dashed lines.	47
4.9 Posterior predictive check using the draws of the detector coefficients a and b . Points with error bars are the polarization weighted sum of event yields. The dashed line is the mean of the predictive values while the solid opaque lines are representative of one simulation draw $a^{(s)}, b^{(s)}$.	48
4.10 Posterior predictive checks $p(A_{\text{rep}} A)$ from a BAYESIAN fit to the event yield asymmetries for all angular bins of the energy bin $1\,250\,\text{MeV} \leq E_\gamma < 1\,310\,\text{MeV}$. The data points in the upper plot are the asymmetry $A(\phi)$, which was additionally fitted using a χ^2 fit (solid line). The goodness of fit is shown using p -values, which give the fraction $T(A_{\text{rep}} > A)$ of replicated samples greater than the original measured value, with propagated statistical error bars on the bottom of each plot. The expected mean value of $T(A_{\text{rep}} > A) = 0.5$ is indicated by the dashed line.	49
4.11 p values generated using all fits. They are centered around their mean at 0.5, which is indicated by the dashed line, and show no bias towards higher or lower values, thus confirming an adequate fit.	50
4.12 Left: relative error $\frac{\sigma_{\text{MCSE}}}{\text{median}[p(\Sigma y)]}$ Right: \widehat{R} associated with the fit parameter Σ . Both are shown for all $11 \cdot 12$ binned fits to the asymmetry $A(\phi)$. The critical values that should not be exceeded are marked by dashed lines.	51

4.13 Left: relative error $\frac{\sigma_{\text{MCSE}}}{\text{median}[P(\Sigma y)]}$ Right: \widehat{R} associated with the fit parameter Σ . Both are shown for all fits. The critical values that should not be exceeded are marked by dashed lines.	52
4.14 Posterior predictive check using the draws of the detector coefficients a and b for the kinematic bin $1250 \text{ MeV} \leq E_\gamma < 1310 \text{ MeV}, 0 \leq \cos \theta < 0.17$. Points with error bars are the polarization weighted sum of event yields. The dashed line is the mean of the predictive values while the solid opaque lines are representative of one simulation draw $a^{(s)}, b^{(s)}$	52
4.15 Final results for the beam asymmetry Σ in η photoproduction off the proton for all kinematic bins obtained with BAYESIAN methods. They are compared with the results of a least squares fit and an unbinned fit as given in reference [Afz19]. All results agree within statistical error bars or within the widths of marginal posterior distributions.	54

List of Tables

1.1	Summary of the particles of the SM	1
1.2	Allowed quantum numbers for the intermediate resonance state N^*/Δ^*	4
3.1	The five most probable decay modes of the η' meson. The most probable further decay with according branching ratio is shown in brackets.[Zyl+20]	11
3.2	Examined MC reactions that were used in sum for the fit	16
3.3	Fit functions and cut ranges for each variable	17
3.4	Total cross sections σ in the energy range 1 500 to 1 800 MeV, branching ratios (BR) to $n\gamma$ final states and maximum acceptance \hat{A} for signal and possible background contributions	23
3.5	Relative loss in signal and background events if a cut on ΔE is applied.	29
4.1	Summary of the complete setting of all toy Monte Carlo experiments for the event based fit. Values and table layout adapted from [Afz19].	45